Controlled synthesis of the antiperovskite oxide superconductor Sr$_{3-x}$SnO

J N Hausmann[1,2,3] , **M Oudah**[1,3], **A Ikeda**[1], **S Yonezawa**[1] and **Y Maeno**[1]

[1] Department of Physics, Graduate School of Science, Kyoto University, Kyoto 606-8502, Japan
[2] Department of Chemistry, Faculty of Mathematics and Natural Sciences, Humboldt-Universität zu Berlin, Brook-Taylor-Strasse 2, Berlin D-12489, Germany

E-mail: maeno@scphys.kyoto-u.ac.jp

CrossMark

Abstract

A large variety of perovskite oxide superconductors are known, including some of the most prominent high-temperature and unconventional superconductors. However, superconductivity among the oxidation state inverted material class, the antiperovskite oxides, was recently reported for the first time. In this superconductor, Sr$_{3-x}$SnO, the unconventional ionic state Sn^{4-} is realized and possible unconventional superconductivity due to a band inversion has been discussed. Here, we discuss an improved facile synthesis method, making it possible to control the strontium deficiency in Sr$_{3-x}$SnO. Additionally, a synthesis method above the melting point of Sr$_3$SnO is presented. We show temperature dependence of magnetization and electrical resistivity for superconducting strontium deficient Sr$_{3-x}$SnO ($T_c \sim 5$ K) and for Sr$_3$SnO without a superconducting transition in alternating current susceptibility down to 0.15 K. Further, we reveal a significant effect of strontium raw material purity on the superconductivity and achieve substantially increased M/M_{Meissner} (~ 1) compared to the highest value reported so far. More detailed characterizations utilizing powder x-ray diffraction and energy-dispersive x-ray spectroscopy show that a minor cubic phase, previously suggested to be another Sr$_{3-x}$SnO phase with a slightly larger lattice parameter, is SrO. The improved characterization and controlled synthesis reported herein enable detailed investigations on the superconducting nature and its dependency on the strontium deficiency in Sr$_{3-x}$SnO.

Keywords: antiperovskite oxide, inverse perovskite oxide, superconductor synthesis, Dirac semimetal, topological superconductor

(Some figures may appear in colour only in the online journal)

1. Introduction

Oxides with perovskite related structures have been playing a major role in the study of superconductivity in the last three decades. Many of the milestones in high temperature superconductivity such as La$_{2-x}$Ba$_x$CuO$_4$ [1, 2], YBa$_2$Cu$_3$O$_{7-x}$ [3] and Bi$_2$Sr$_2$CaCu$_2$O$_{8+\delta}$ [4] as well as the unconventional superconductor Sr$_2$RuO$_4$ [5] with evidence for spin-triplet superconductivity [6, 7] belong to this class of oxides. However, the symmetrically equivalent, but oxidation state inverted analog, the inverse perovskite or antiperovskite (AP) oxide, was much less in the focus of investigation by the scientific community, probably due to its instability in air. The first superconductor among AP oxides, Sr$_{3-x}$SnO, was reported very recently by our group [8]. Potentially, this discovery can be the beginning of the emergence of a new promising family of AP oxide superconductors [9–18].

In general, two formulae for cubic AP oxides are known: M_3^+O$^{2-}A^-$ and $M_3^{2+}A^{4-}$O^{2-}, see figure 1. In both cases O^{2-} is coordinated octahedrally by six M, whereas A is coordinated cuboctahedrally by twelve M. In the first case, materials are known where M is an alkaline metal or silver and A a halogen or gold [9–18]. In the latter case, materials are known where M is an alkaline earth metal or lanthanoid and A indium or a group 14 element [19–25].
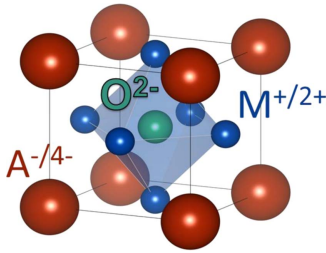
[3] Equally contributed.

Figure 1. General unit cell for cubic antiperovskite oxides of the formulae $M_3^+O^{2-}A^-$ and $M_3^{2+}A^{4-}O^{2-}$.

Band structure calculations of AP oxides of the latter case, containing tin or lead as *A* and alkaline earth metals as *M*, have revealed the presence of six equivalent three-dimensional Dirac electrons, located in the very vicinity of the Fermi surface in some of these compounds like Sr_3SnO or Ca_3PbO [26, 27]. The emergence of the Dirac cones is related to a band inversion between the valence band, mainly originating from the *p* orbitals of tin or lead, and the conduction band, mainly originating from the *d* orbitals of the alkaline earth metal. These band structures imply nearly closed shell ionic compounds. This is consistent with the observed distances between the alkaline earth and oxygen ions in the crystal structures [8, 20]. Thus, the unusual ionic states of Sn^{4-} and Pb^{4-} are realized. Furthermore, it was predicted that a new topological phase, protected by mirror symmetry of the crystal, is present in some members of this family of AP oxides including Sr_3SnO [28, 29]. Recently, cone-like band dispersion in good agreement with the electronic structure calculations [28] were observed by soft x-ray angle-resolved photoemission spectroscopy of Ca_3PbO single crystals [30]. This strongly supports that some AP oxides host 3D Dirac fermions.

The first AP oxide superconductor, $Sr_{3-x}SnO$ with a transition temperature T_c of 5 K, was reported very recently by our group [8]. As the parity of the Cooper pairs reflects the orbital texture of the underlying Fermi surface, $Sr_{3-x}SnO$ is a candidate for topological superconductivity, due to the mixing of the Sn-5*p* and Sr-4*d* bands at the Fermi level. A recent first-principles study on the superconducting properties of Sr_3SnO predicted it to be a topological superconductor with a T_c of 8.38 K [31]. Early samples of our group showing superconductivity had a $M/M_{Meissner}$ of 0.32 without demagnetization correction. Such a fraction is evaluated by the ratio of observed magnetization based on the sample mass divided by the expected magnetization with 100% Meissner effect, $M/M_{Meissner}$. These early samples suffered from uncontrolled evaporation of strontium during the synthesis [8]. In fact, superconducting samples contained two cubic phases, whose lattice parameters were different by only 0.02 Å. Later we found that the evaporation can be suppressed by synthesizing the samples under argon pressure. A magnetization curve of a sample synthesized under argon pressure was presented in that report. That magnetization curve demonstrated bulk superconductivity with $M/M_{Meissner}$

of 0.62. However, its synthesis was not discussed and no powder x-ray diffraction (pXRD) data was presented.

In this paper, we present details of the utilization of argon pressure to suppress the strontium evaporation as well as a synthesis of Sr_3SnO from temperatures above its melting point. We show pXRD, energy-dispersive x-ray spectroscopy (EDX), direct current (DC) magnetization and resistivity data for stoichiometric Sr_3SnO and deficient $Sr_{3-x}SnO$ samples. The analysis of the pXRD data of these improved samples makes it possible to identify the two phases present in the reported superconducting sample, identifying one as SrO and the other one as $Sr_{3-x}SnO$. This is further supported by EDX measurements. The single-phase stoichiometric Sr_3SnO samples do not show any superconducting transition in alternating current (AC) susceptibility down to 0.15 K and exhibit semiconducting behavior in contrast to metallic behavior for the strontium deficient sample in the temperature dependent resistivity. Further, we reveal a strong effect of small amounts of non-magnetic impurities in the strontium starting material on the superconductivity. The magnetic shielding of a strontium deficient '$Sr_{2.5}SnO$' sample exhibits $M/M_{Meissner}$ of essentially 1 at 2 K with a superconducting onset of 5.4 K.

2. Experimental

2.1. Sample synthesis

The samples were synthesized following our previously published procedure (Method A) and with the modified Methods B and C, as summarized in table 1.

For all procedures, the strontium (specification below) and the SnO powder (Furuuchi, 99.9%, 169.4 mg, defined as 1.0 molar equivalent (eq.)) were loaded inside an argon filled glovebox into a crucible. After sealing the crucible in quartz tubes under vacuum (pressure $p < 10$ Pa) or argon pressure, the quartz tubes were placed at an approximately 45° angle into a box furnace and the appendant temperature program was applied. After the water-quenching, the quartz tubes were opened, stored and prepared for further experiments inside an argon filled glovebox.

2.1.1. Method A. Synthesis under vacuum. The synthesis of Samples A-1 and A-2 was performed in alumina crucibles (SSA-S, $11 \times 42 \times 1.5$ mm) sealed in quartz tubes under vacuum. For Sample A-1 clean cut strontium chunks (Furuuchi, chunks stored in oil, 99.9%, 413.3 mg, 3.75 eq. with respect to the amount of SnO) and for Sample A-2 clean cut strontium chunks (Furuuchi, chunks stored in oil, 99.9%, 330.6 mg, 3.0 eq.) were used. The sealed quartz tubes were heated to 800 °C over 3 h and kept at 800 °C for 3 h before water-quenching. In both cases a metallic shining black surface on the inside of the quartz tube wall could be observed, clearly indicating an evaporation of a compound outside of the crucible. As the evaporating strontium leaves the crucible and reacts with the inside wall of the quartz tube, the weight loss of the crucible is related to the amount of

Table 1. Summary of the most significant synthesis parameters and the superconducting volume fraction estimated from DC magnetization $M(T)$ data of six different representative batches.

Sample name	Product	Starting composition	Atmosphere at room temperature	T_{max} (°C)	Strontium purity (%)	$M/M_{Meissner}$	Estimated volume fraction (%)[a]
A-1	Sr_3SnO	3.75 Sr + SnO	Vacuum	800	99.9	<0.015	<1.0
A-2	$Sr_{3-x}SnO$[b]	3.0 Sr + SnO	Vacuum	800	99.9	0.23	15
B-1	Sr_3SnO	3.0 Sr + SnO	30 kPa Ar	825	99.9	0	0
B-2	'$Sr_{2.5}SnO$'	2.5 Sr + SnO	30 kPa Ar	825	99.9	0.64	43
B-3	'$Sr_{2.5}SnO$'	2.5 Sr + SnO	30 kPa Ar	825	99.99	1.05	70
C	Sr_3SnO	3.1 Sr + SnO	23 kPa Ar	1200	99.99	0	0

[a] For simplicity, we assume demagnetization correction for a spherical shaped sample.

[b] The value of x in Sample A-2 is estimated from the measured Hall coefficient and is about 0.3 [8].

evaporated Sr. Weighing the crucible with the sample inside before and after the reaction yielded a weight loss corresponding to 12%–25% of the total strontium loading. Considering the uncertainly in weight loss, the value of x in Sample A-2 is estimated from the measured Hall coefficient and is about 0.3 [8].

2.1.2. Method B. Synthesis under argon pressure. The synthesis of Samples B-1, B-2 and B-3 was performed in alumina crucibles (SSA-S, $11 \times 42 \times 1.5$ mm) sealed in quartz tubes under 30 kPa of argon pressure at room temperature. For Sample B-1 clean cut strontium chunks (Furuuchi, chunks stored in oil, 99.9%, 331.1 mg, 3.00 eq.), for Sample B-2 clean cut strontium chunks (Furuuchi, chunks stored in oil, 99.9%, 271.6 mg, 2.5 eq.) and for Sample B-3 dendritic strontium pieces (Sigma Aldrich, dendritic pieces stored under argon, 99.99%, 271.6 mg, 2.5 eq.) were used. The sealed quartz tubes were heated to 825 °C over 3 h and kept at 825 °C for 3 h before quenching.

2.1.3. Method C. Synthesis at temperatures above the melting point of Sr_3SnO. The synthesis of Sample C was performed in tantalum crucibles (Japan Metal Service Co. Ltd, 99.95%, $14 \times 35 \times 0.5$ mm³) sealed under 23 kPa of argon pressure. Dendritic strontium pieces (Sigma Aldrich, dendritic pieces stored under argon, 99.99%, 341.6 mg, 3.1 eq.) were used. The sealed quartz tubes were heated to 825 °C over 40 min and kept at 825 °C for 20 min. Subsequently they were heated up to 1200 °C in 30 min and kept there for 2.5 h to melt the Sr_3SnO before quenched in water. After the water-quenching, the samples were heated up to 900 °C over 1 h and kept there for 48 h to improve the homogeneity and crystallinity before they were quenched in water for a second time.

2.2. Sample characterization

2.2.1. pXRD. The pXRD measurements for Samples B-1 and B-2 were performed at room temperature with a diffractometer (Bruker AXS, D8 Advance) utilizing Cu-K$_\alpha$ radiation (1.54 Å) selected by a nickel-monochromator. Inside an argon filled glovebox these samples were crushed lightly and the obtained powder placed in the center of the XRD stage, then pressure was applied with a flat glass object to

obtain a straight surface and finally the samples were covered with a 12.5 μm thick polyimide film (DuPont, Kapton) attached to the sample stage by distributing vacuum grease (Dow Corning Toray, high vacuum grease) in the form of a circle around the sample and pressing the polyimide film on top of it. Samples prepared in this fashion were stable in air for a few hours, before they slowly decomposed into tin and $Sr(OH)_2 \cdot nH_2O$. Typical pXRD measurement times were 30 to 220 min.

2.2.2. Synchrotron pXRD. Additional pXRD measurements for Sample C were performed at room temperature using synchrotron radiation with a wavelength of $\lambda = 0.42073$ Å on the BL02B2 beam line at SPring-8 (Hyogo, Japan). The samples were finely ground into powder, and then inserted into a fused-silica capillary tube of inner diameter 0.5 mm under nitrogen atmosphere. During data collection, the tube was continuously rotated to minimize the impact of any preferred orientation, and the scans were obtained over 3 min for each sample.

2.2.3. EDX. EDX spectra were collected using a commercial detector (AMETEK Inc., model: Element) equipped on a scanning electron microscope (SEM; KEYENCE, model: VE-9800). In a glove box filled with argon, the sample powder was placed on a metallic stage with a conductive double-sided tape made from carbon and aluminum (Nisshin EM Co., Ltd, catalog number: 7321). The samples were exposed to air during the evacuation inside the SEM. Incident electrons with an energy of 15 keV and spot size of 16 were used. To construct the element mappings, we integrated 16 frames for each sample. Every pixel of a frame was obtained by collecting the emitted x-rays for 100 ms.

2.3. Physical properties

2.3.1. MPMS. A commercial superconducting quantum interference device magnetometer (Quantum Design, MPMS) was used to measure the DC magnetization M. Samples were covered with grease in an argon environment, then placed inside plastic straws for measurement. Degaussing was performed prior to measurement to ensure the accuracy of the applied field. Furthermore, the remnant field inside the MPMS was

occasionally measured using a reference sample (Pb, 99.9999%), and found to be $\leqslant 0.1$ mT after degaussing.

2.3.2. Resistivity. The resistivity measurement was performed using a four-probe method from 1.8 to 300 K. A sample with a typical size of $2.0 \times 2.0 \times 0.6$ mm^3, and 50 μm diameter gold wires were attached using silver epoxy (Epoxy Technology, H20E) inside an argon filled glovebox. A layer of vacuum grease (Apiezon, N-grease) was applied over the samples inside the glovebox to protect them from contact with air. The samples were cooled during resistivity measurement using a commercial apparatus (Quantum Design, PPMS).

3. Results and discussion

3.1. Synthesis and phase characterization

Table 1 above gives an overview of the synthesis parameters and superconductivity of the samples presented in this report. Samples synthesized under vacuum, as in our previous report (Method A) [8], show a metallic shining black surface on the inside of the quartz tube. Using pXRD we identified this black surface as different Sr$_x$Si$_y$ phases. Therefore, evaporated strontium reduces the SiO$_2$ of the quartz tube to form this dark surface. The amount of strontium evaporating varies from 12% to 25% of the total strontium loading, as determined by weighing the crucible before and after the reaction (see the experimental section for details). This evaporation makes it impossible to control the strontium content in the final product.

We increased the strontium loading to compensate for the evaporated material to synthesize a pure stoichiometric Sr$_3$SnO phase to compare its superconducting and electrical properties to the ones of Sr$_{3-x}$SnO of our previous report [8]. In Sample A-1 evaporation and strontium excess compensated each other, as deduced from the final weight of product in the crucible. The pXRD of this sample exhibits only one single cubic phase and no impurities. Therefore, it is considered as stoichiometric Sr$_3$SnO. However, most probably due to a low crystallinity the peaks are very broad, and hence the presence of an additional minor cubic phase with a slightly larger lattice parameter cannot be excluded certainly.

The evaporation can be suppressed through sealing the quartz tubes under an argon atmosphere of 30 kPa at room temperature (Method B), corresponding to 110 kPa at 825 °C with an assumption of ideal gas behavior. Due to the successful suppression, it is now possible to control the strontium content in the final product and to investigate the dependence of the superconductivity on the strontium deficiency as well as the emergence of the second cubic phase (figure 2(c)). Detailed data on the relation between strontium deficiency and superconductivity will be published elsewhere. Samples synthesized with 3 eq. or more of strontium are single phased and show a high crystallinity (figure 2(b)). Decreasing the strontium loading leads to the emergence of a second cubic phase with a 0.02 Å larger lattice parameter (figure 2(c)). The

difference in the lattice parameters of both phases stays at 0.02 Å, independently of the strontium loading. The diffractogram presented in our previous report showed two similar cubic phases. Then, we suspected that this phase splitting is due to different strontium contents in the two different Sr$_{3-x}$SnO phases. As the new samples in this report synthesized under argon pressure have an improved crystallinity, resulting in narrower peak shapes in the pXRD, the peaks belonging to the two different cubic phases overlap less and can be analyzed more carefully.

A diffractogram of such a new Sample B-2 is shown in figure 2(c). The lattice parameter of the main cubic phase is 5.137 Å and the one of the minor phase 5.160 Å. Recently, a lattice parameter of 5.139 Å for Sr$_3$SnO single crystals was reported [25], agreeing well with our main phase. The lattice parameter of the minor phase agrees with 5.160 Å, reported for SrO [32]. Additionally, the peak intensity ratios of the (1 1 1), (2 0 0), (2 2 0) and (3 1 1) peaks are expected to be different in Sr$_3$SnO and SrO. The leftmost peak of the three peaks present for each of these four diffraction planes belongs exclusively to the minor phase, see the peaks marked with red K$_{\alpha1}$ in figures 2(c$_3$) and (c$_4$) as an example for the (0 2 2) and (3 1 1) diffraction planes. The intensity ratios of these leftmost peaks fit to the one expected for SrO and the one of the rightmost peaks, originating exclusively from the major phase, to the one of Sr$_3$SnO. To gain further support for the presence of SrO, one of the low intensity peaks (2 1 1), expected to be only present in the primitive cubic Sr$_3$SnO and not in face centered cubic SrO, was measured exclusively overnight; see the magnified peak in figure 2(c$_2$). No splitting in two phases is present in this peak, indicating that a second primitive cubic is not present, but a face centered cubic phase is. Furthermore, the problem of alkaline earth oxide impurities is reported in literature known for the synthesis of bulk [23, 25] and thin film [33] antiperovskite oxides. Therefore, we conclude that the face centered cubic phase is SrO.

One peak for SnO (superconducting only under pressure) [34] and four very small peaks of tin ($T_c = 3.7$ K) [35] in figure 2(c) are marked with an x and asterisks, respectively (PDF-2 database: PDF000130111 for SnO and PDF030650296 for tin). However, due to the small intensity an unambiguous identification by pXRD is not possible. The EDX results presented in figure 3(a) show a small area containing only tin. Additionally, the DC magnetization $M(T)$ curves occasionally show a very small anomaly around 3.7 K. Hence, we conclude a small tin impurity is very likely. This tin impurity in the pXRD may also originate from a minor decomposition of Sr$_{3-x}$SnO into tin and Sr(OH)$_2$·nH$_2$O. For the magnetization measurements, performed at low temperatures in an air-free environment, such a decomposition is not expected and in fact most of the samples do not show a superconducting signal from tin ($T_c = 3.7$ K).

Due to the SrO and tin impurity the precise stoichiometry of the final AP oxide phase is challenging to determine. The strontium deficiency might be slightly more than expected from the initial strontium loading. Furthermore, an oxygen deficiency is possible. However, considering that Sr$_3$Sn
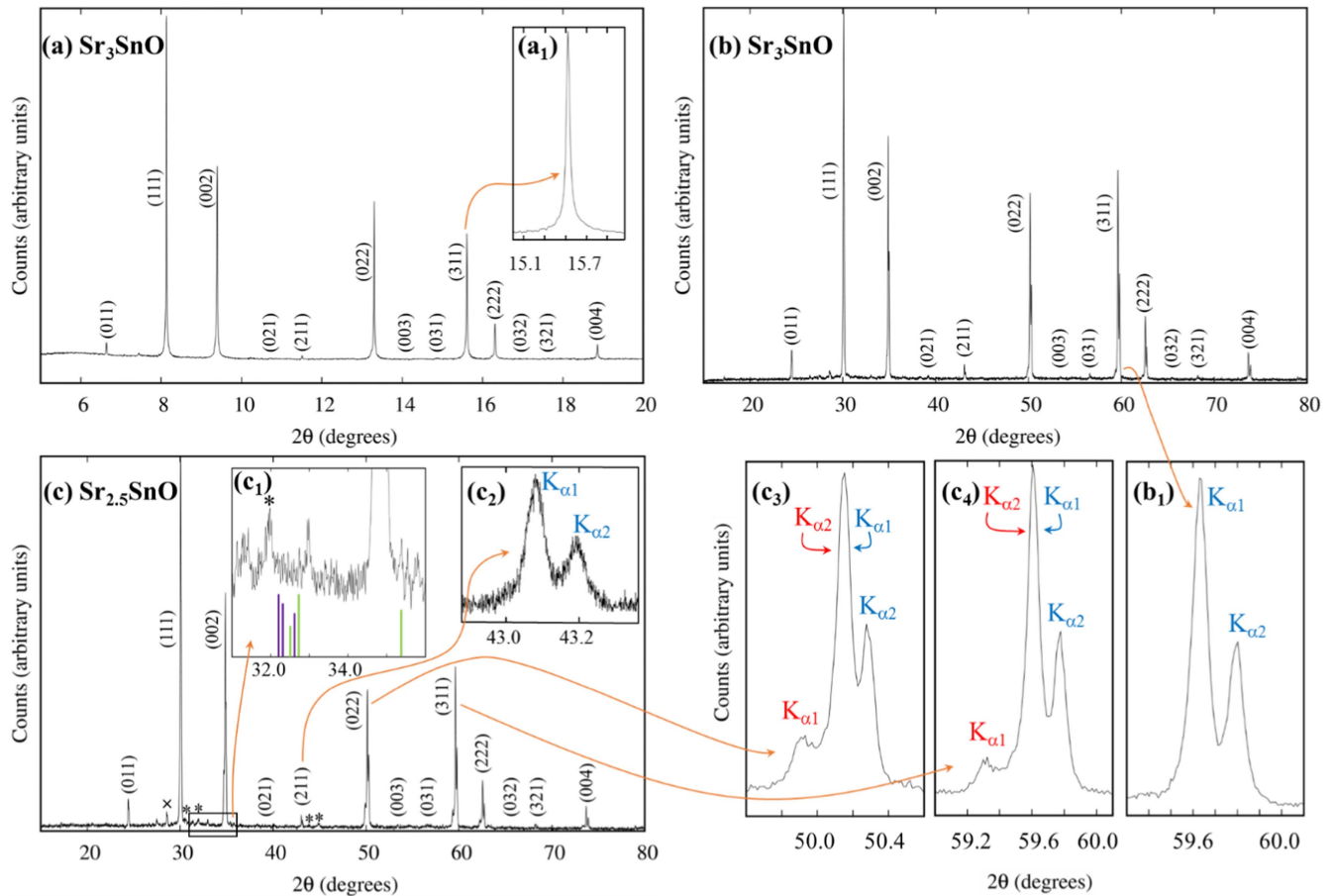
Figure 2. Powder x-ray diffraction patterns of $Sr_{3-x}SnO$ at room temperature. The intensities are in linear scales. The diffraction pattern (a) was obtained at the synchrotron-radiation facility SPring-8 with an x-ray wavelength of $\lambda = 0.42073$ Å. The diffraction patterns (b) and (c) were obtained with a laboratory-based diffractometer utilizing Cu-K_α ($\lambda = 1.54$ Å) radiation. (a) and (b) are for stoichiometric and non-superconductive Sr_3SnO of Sample C and B-1, respectively. (c) is for the superconductive '$Sr_{2.5}SnO$' Sample B-2. The insets are magnifications of certain peaks or areas. The green and purple bars in inset (c_1) indicate the expected position and intensity (PDF-2 database: PDF010734901 for $SrSn_3$ and PDF010723942 for $SrSn_4$) of the three most pronounced peaks of the only two known superconducting Sr–Sn-alloys $SrSn_3$ and $SrSn_4$, respectively. For the diffractograms of the stoichiometric batches (a) and (b) only the primitive cubic Sr_3SnO phase can be observed. For (b) and (c) a splitting of the peaks due to $K_{\alpha 1}$ and $K_{\alpha 2}$ radiation is present. The additional splitting in the peaks of (c) is due to an additional face centered cubic SrO phase. The peaks originating from the SrO phase ($a = 5.160$ Å) are indicated by $K_{\alpha 1 \text{ or } 2}$ in red in the insets (c_3) and (c_4). The ones originating from the '$Sr_{2.5}SnO$' phase ($a = 5.137$ Å) are indicated by $K_{\alpha 1 \text{ or } 2}$ in blue in the insets (c_2), (c_3), (c_4) and (b_1). In (c) the peaks of a SnO and tin impurity (PDF-2 database: PDF000130111 for SnO and PDF030650296 for tin) are marked by an x and asterisks, respectively.
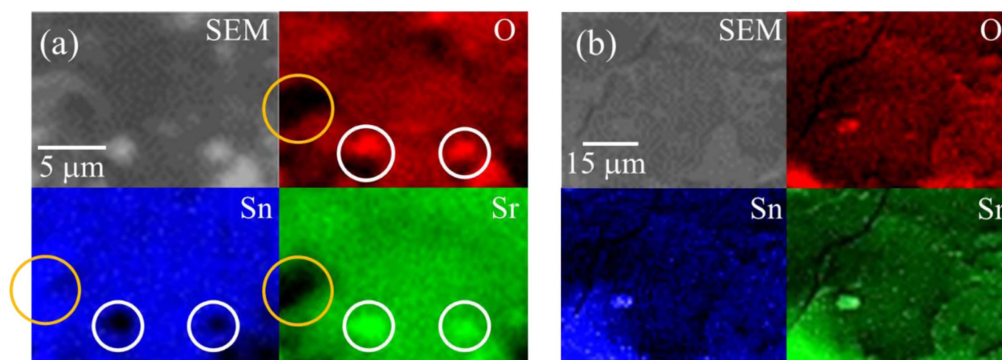

Figure 3. SEM and EDX images of '$Sr_{2.5}SnO$' of Sample B-2 (a) and 'Sr_3SnO' of Sample C (b). The air sensitive samples were exposed to air while vacuum was applied to the SEM/EDX chamber. Therefore, no flat surfaces and reliable quantitative analysis could be obtained. The gray images at the top left panels of (a) and (b) are the SEM images and the other three pairs are the EDX images of the same areas. The oxygen distribution is red, the tin one blue and the strontium one green. All three elements are distributed in a similar way in (a) and (b), indicating a strong dominance of the $Sr_{3-x}SnO$ phase. In (a) are some areas with different element ratios, indicating impurities. The white circles in (a) indicate a region containing almost only strontium and oxygen. The orange circles an area containing almost only tin.

without oxygen could not be synthesized despite attempts during work on Sr–Sn phase diagrams [19, 20], a significant oxygen deficiency is unlikely. It is possible that small amounts of oxygen are provided through a reaction with the alumina crucible or from another unknown source. Due to these uncertainties in strontium deficient samples, their molecular formula is set in quotation marks in this report.

Two Sr–Sn alloys are known to be superconducting, SrSn$_3$ ($T_c = 5.4$ K) [36] and SrSn$_4$ ($T_c = 4.8$ K) [37]. The green and purple bars in the inset (c_1) of figure 2 indicate the expected position and intensity (PDF-2 database: PDF010734901 for SrSn$_3$ and PDF010723942 for SrSn$_4$) of the three most pronounced peaks of SrSn$_3$ and SrSn$_4$, respectively. The peak positions anticipated for SrSn$_4$ do not match those of the experimentally observed pXRD. Further, if we assume that the main impurity peaks observed at $2\theta = 32.99°$ and $35.80°$ are from SrSn$_3$, the lattice constants a and c would be shorter than the reported values by 16% and 2.9%, respectively. These large differences, especially in a, suggest that the impurity peaks do not correspond to SrSn$_3$. Thus, the presence of significant amounts of crystalline SrSn$_3$ and SrSn$_4$ impurities is unlikely.

3.2. Element distribution on the surface

SEM and EDX spectroscopy was performed on 'Sr$_{2.5}$SnO' of Sample B-2, see figure 3(a). Due to the inevitable short-time exposure of the sample to air in our apparatus, we could not maintain flat surfaces and reliable quantitative results for the element ratios. However, the EDX images clearly show that the distributions of oxygen (red), tin (blue) and strontium (green) are very similar in a major part of the sample's surface, supporting the dominance of the Sr$_{3-x}$SnO phase and excluding a significant amorphous impurity with a different composition. Figure 3(a) represents the area where impurity phases are clearly seen. The orange circles mark an area, containing only tin and the white circles an area containing strontium and oxygen. These EDX results are in accordance to our pXRD data, see figure 2(b), which shows Sr$_{3-x}$SnO as dominant phase with SrO oxide and tin as impurities. In general, much more areas containing only strontium and oxygen could be identified by EDX than areas containing only tin, as also expected from the pXRD data.

3.3. Notes on synthesis conditions

A brief screening of reaction temperatures in the range of 800 °C–1000 °C and reaction times from 1 h to 48 h was performed. Since no product formation is observed at temperatures below the melting point of strontium ($T_m = 777$ °C), we deduce that the reaction of strontium and SnO to Sr$_{3-x}$SnO is promoted by the melting of strontium. No significant differences is observed in the pXRD and DC magnetization $M(T)$ data for higher reaction temperatures. We choose a maximum furnace temperature of 825 °C instead of 800 °C, in order to guarantee the complete melting of the strontium in our setup. We choose a

reaction time of 3 h, as further sintering does not result in any changes in the pXRD and DC magnetization $M(T)$ data.

The stoichiometric sample A-1 still shows M/M_{Meissner} of less than 0.015 at 2 K, indicating inhomogeneity of the strontium distribution with some deficient domains. To obtain more homogeneous materials with an improved crystallinity, Sr$_3$SnO was synthesized by heating the stoichiometric starting materials above $T_m(\mathrm{Sr_3SnO}) = 1080$ °C and with an argon pressure of 23 kPa at room temperature. However, the molten Sr$_3$SnO reacts with the alumina crucible, forming Sr$_x$(Al$_y$O$_z$). Thus, tantalum crucibles were used instead. Initially, slow cooling through the melting point was tried to grow single crystals. However, crystals with a sufficient size were not obtained and noticeable amounts of SrSn ($T_m = 1140$ °C) as well as SrO were present in all these samples. Therefore, a different method was used in which samples were water-quenched from 1200 °C and then sintered at 900 °C for 48 h to improve their crystallinity. Samples synthesized in this way with stoichiometric or slightly over stoichiometric strontium loadings do not show any superconductivity down to 0.15 K in AC susceptibility measurements, indicating a high homogeneity in the strontium distribution. A high energy pXRD of such a sample C is shown in figure 2(a). It is free of any impurities and the peak shape indicates high crystallinity. Figure 3(b) shows EDX images of the oxygen (red), tin (blue) and strontium (green) distribution. Although the EDX samples suffered from a slight exposure to air, all three elements are distributed homogeneously in most of the areas supporting the presence of a clean Sr$_3$SnO phase, as indicated by the pXRD data of figure 2(a).

As quenching Sr$_3$SnO from above its melting point was successful for synthesizing stoichiometric samples with a homogenous strontium distribution, we attempted the same method for strontium deficient samples. However, we found that at temperatures above the melting point deficient Sr$_{3-x}$SnO decomposes into Sr$_x$Sn$_y$, SrO and stoichiometric Sr$_3$SnO. Hence, this procedure is not suitable for the synthesis of superconducting strontium deficient samples. Successful synthesis of large single crystals is reported in a strontium-rich environment [25]. These crystals are not expected to include sufficient deficiency required for superconductivity in Sr$_{3-x}$SnO. Further, the formation of impurities for less strontium rich environments is mentioned. As we also observe that 'Sr$_{2.5}$SnO' decomposes when heated above its melting point, the promising synthesis of strontium deficient Sr$_{3-x}$SnO single crystals seems challenging.

Another crucial aspect for the synthesis of superconducting Sr$_{3-x}$SnO is a high purity of the strontium raw material, as discussed in the following section.

3.4. Superconductivity and normal state properties

Figure 4 shows DC magnetization data $M(T)$ of stoichiometric Sr$_3$SnO sample (Sample B-1), as well as 'Sr$_{2.5}$SnO' samples synthesized using strontium raw materials of different purities (99.9% for Sample B-2 and 99.99% for Sample B-3). The
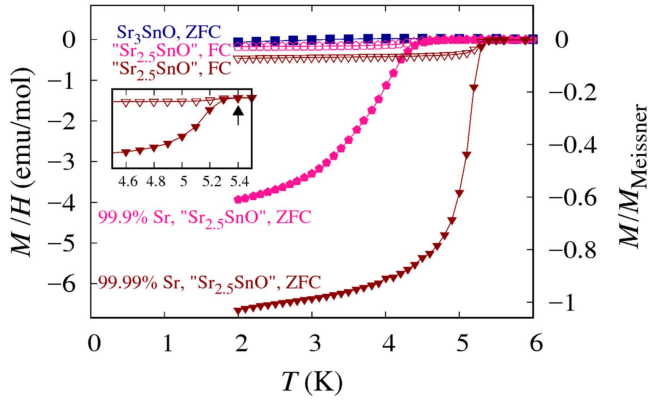
Figure 4. Magnetization under zero field cooling (ZFC) with an applied field of 2 mT of Sr_3SnO of Sample B-1 (blue squares), and under ZFC as well as field cooling (FC) of '$Sr_{2.5}SnO$' of Sample B-2 (pink pentagons) and Sample B-3 (brown triangles). The vertical scale on the right indicates the ratio of the observed magnetization to that for the full Meissner signal, $M/M_{Meissner}$. Stoichiometric Sr_3SnO is not superconducting. The $M/M_{Meissner}$ of '$Sr_{2.5}SnO$' increases significantly with an increased purity of the strontium raw material. The inset is a magnification, showing the onset of the diamagnetic signal.

Figure 5. Electrical resistivity ρ as a function of temperature of polycrystalline chunks of Sr_3SnO of Sample A-1 in blue (arrow to the right) and of $Sr_{3-x}SnO$ ($x \sim 0.3$) of Sample A-2 in red (arrow to the left). For stoichiometric Sr_3SnO, the drop at 3.8 K is most likely due to a metallic tin impurity ($T_c = 3.7$ K). For hole doped $Sr_{3-x}SnO$, $\rho(T)$ is metallic with the a superconducting transition below 5 K.

synthesis methods of B-2 and B-3 are identical and their pXRD data show no significant differences. The curve for the zero-field-cooling (ZFC) process of Sample B-2 shows a magnetic flux expulsion corresponding to $M/M_{Meissner}$ of 0.64 at 2 K with an onset of 4.7 K. The ZFC curve of Sample B-3 reveals $M/M_{Meissner}$ of 1.05 with an onset of 5.4 K. Both ratios clearly indicate bulk superconductivity of the main '$Sr_{2.5}SnO$' phase.

'$Sr_{2.5}SnO$' samples using strontium raw material of 99% purity[4] were also synthesized in the same procedure as for B-2 and B-3, and they exhibit equivalent crystallinity in pXRD. Remarkably, these samples do not exhibit any superconducting transition in the DC magnetization $M(T)$ down to 2 K. These results suggest that even non-magnetic impurities incorporated in '$Sr_{2.5}SnO$' are detrimental to superconductivity. Since a high sensitivity to non-magnetic impurities is known for some unconventional superconductors such as Sr_2RuO_4 [38], the present results motivate further studies of the impurity effect in the superconductivity of $Sr_{3-x}SnO$.

The diamagnetic signals in the field-cooling curves in figure 4 of Samples B-2 and B-3 are much less pronounced compared with those in the ZFC curves, as expected for a type-II superconductor due to flux pinning. In the ZFC curve of Sr_3SnO (Sample B-1) no sizeable diamagnetic transition is present down to 2 K. Furthermore, a AC susceptibility measurement down to 0.15 K did not reveal any superconducting transition. These results clearly indicate that only strontium deficient $Sr_{3-x}SnO$ is superconducting.

The blue curve in figure 5 shows the dependence of the electrical resistivity ρ on the temperature of polycrystalline chunks of Sr_3SnO (Sample A-1). It indicates weak
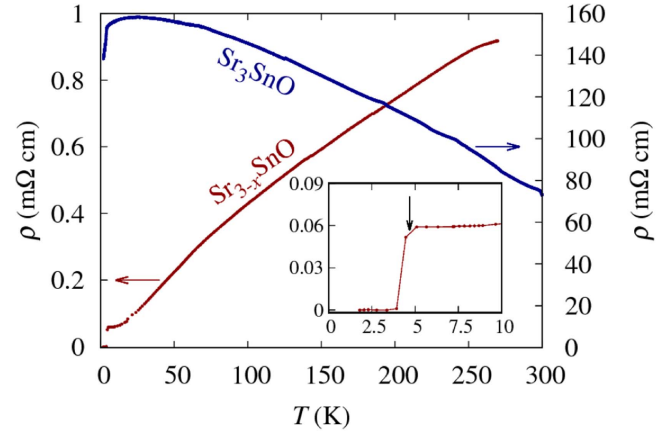
semiconducting temperature dependence with the value at 10 K to be 0.154 Ωcm. This is consistent with the first-principles band calculations of our recent report, implying an isolated gapped Dirac cone in the very vicinity of the Fermi energy [8]. The presence of another hole pocket around the R point, as indicated by a first-principles band calculation by Hsieh et al [28], stands in contrast to this result. The absence of such a hole pocket around the R point further supports our claim that the Cooper pairs are formed on the Fermi surface originating from the Dirac points, and therefore could results in unconventional superconducting properties [8]. The temperature dependence of ρ is metallic for $Sr_{3-x}SnO$ (Sample A-2, figure 5 red curve) with the value at 10 K to be 65 $\mu\Omega$ cm. This is expected, as the Fermi energy should be shifted downwards due to the heavy hole doping caused by the strontium deficiency. For this sample ρ drops sharply with an onset of 4.8 K and reaches zero at 4.5 K, and thus further supports bulk superconductivity of strontium deficient $Sr_{3-x}SnO$. For Ca_3SnO and Ca_3PbO, predicted to have a similar band structure with small band gaps [28], metallic temperature dependence of ρ was also observed for samples synthesized under vacuum [39]. In the Sr_3SnO Sample A-1, the resistivity seems to saturate at $\sim$25 K followed by a slight drop down to $\sim$5 K and a sharp drop at 3.8 K. This drop is most likely due to a small inclusion of metallic tin ($T_c = 3.7$ K) in our sample. The scattering is expected to increase in the hole-doped $Sr_{3-x}SnO$ sample, but the increases in number of carriers with doping is more significant, which is demonstrated by the 1000 times decrease in ρ of the metallic $Sr_{3-x}SnO$ sample compared with the semiconducting Sr_3SnO sample. These results show the significant effect of doping in this material, and may arise from the Dirac dispersion observed in the band calculations.

---

[4] Rare Metallic, impurities according to the manufacturer: Ca < 0.13%, Ba < 0.16%, Mg: 0.005%, Si: 0.0021%, Fe: 0.0008%, Na: 0.0026%.

4. Conclusion

The synthesis Method B presented in this report, namely heating at 825 °C for 3 h with an argon pressure of at least 30 kPa at room temperature, with a molar Sr:SnO ratio of 2.5 in $Sr_{3-x}SnO$ and using a strontium raw material with the purity of 99.99%, succeeds in producing bulk polycrystalline $Sr_{3-x}SnO$ with $M/M_{Meissner}$ of around 1. Furthermore, the magnitude of the strontium deficiency can be controlled and we demonstrate the absence of superconductivity in stoichiometric Sr_3SnO. Additionally, we performed a more detailed characterization of the superconducting '$Sr_{2.5}SnO$' material. With this synthesis method established and the improved understanding of the material the nature of the superconductivity and the dependence of it on the strontium deficiency in $Sr_{3-x}SnO$ can be investigated in more detail in the future.

ORCID iDs

J N Hausmann https://orcid.org/0000-0002-2336-3600

References

[1] Bednorz J G and Müller K A 1986 Possible high T_c superconductivity in the Ba–La–Cu–O system *Z. Phys.* B **64** 189–93

[2] Michel C, Hervieu M, Borel M M, Grandin A, Deslandes F, Provost J and Raveau B 1987 Superconductivity in the Bi–Sr–Cu–O system *Z. Phys.* B **68** 421–3

[3] Wu K M, Ashbum J R, Tomg C J, Hor P H, Meng R L, Gao L, Huang Z J, Wang Y Q and Chu C W 1987 Superconductivity at 93 K in a new mixed-phase Y–Ba–Cu–O compound system at ambient pressure *Phys. Rev. Lett.* **58** 908–10

[4] Maeda H, Tanaka Y, Fukutumo M and Asano T 1988 A new high-T_c oxide superconductor without a rare earth element *Japan. J. Appl. Phys.* **27** L209

[5] Maeno Y, Hashimoto H, Yoshida K, Nishizaki S, Fujita T, Bednorz J G and Lichtenberg F 1994 Superconductivity in a layered perovskite without copper *Nature* **372** 532–4

[6] Ishida K, Mukuda H, Kitaoka Y, Asayama A, Mao Z Q, Mori Y and Maeno Y 1998 Spin-triplet superconductivity in Sr_2RuO_4 identified by ^{17}O Knight shift *Nature* **396** 658–60

[7] Maeno Y, Kittaka S, Nomura T, Yonezawa S and Ishida K 2012 Evaluation of spin-triplet superconductivity in Sr_2RuO_4 *J. Phys. Soc. Japan* **81** 011009

[8] Oudah M, Ikeda A, Hausmann J N, Yonezawa S, Fukumoto T, Kobayashi S, Sato M and Maeno Y 2016 Superconductivity in the antiperovskite Dirac-metal oxide $Sr_{3-x}SnO$ *Nat. Commun.* **7** 13617

[9] Zintl E and Morawietz W 1938 Orthosalze von Sauerstoffsäuren *Z. Anorg. Allg. Chem* **236** 372–410

[10] Sabrowsky H, Paszkowski K, Reddig D and Vogt P 1988 Na_3OCl and Na_3OBr the first alkali metal chalcogenide halides *Z. Naturforsch.* **43b** 238–9

[11] Jansen M 1977 Neue untersuchungen an Na_3NO_3 *Z. Anorg. Allg. Chem.* **435** 13–20

[12] Sitta S, Hippler K, Vogt P and Sabrowsky H 1991 Kristallstruktur von gelbem K_3OBr *Z. Anorg. Allg. Chem.* **597** 197–200

[13] Sitta S, Hippler K, Vogt P and Sabrowsky H 1991 Crystal structure of K_3OI *Z. Kristallogr. Cryst. Mater.* **196** 193–6

[14] Feldmann C and Jansen M 1995 Darstellung und kristallstruktur von Cs_3ClO *Z. Naturforsch.* **50b** 1415–6

[15] Feldmann C and Jansen M 1995 Zur kristallchemischen ähnlichkeit von aurid-und halogenid-ionen *Z. Anorg. Allg. Chem.* **621** 1907–12

[16] Sabrowsky H, Feldbaum-Moller E, Fischer K, Sitta S, Vogt P and Winter V 1996 Die Kristallstrukturen von alpha-und beta-K_3OCl *Z. Anorg. Allg. Chem.* **622** 153–6

[17] Feldmann C and Jansen M 1995 Zur Kenntnis neuer ternärer oxide mit anionischem gold *Z. Anorg. Allg. Chem.* **621** 201–6

[18] Zhao Y and Daemen L L 2012 Superionic conductivity in lithium-rich anti-perovskites *J. Am. Chem. Soc.* **134** 15042–7

[19] Widera A and Schäfer H 1980 Übergangsformen zwischen zintlphasen und echten salzen: die verbindungen A_3BO (mit $A = Ca$, Sr, Ba und $B = Sn$, Pb) *Mater. Res. Bull.* **15** 1805–9

[20] Widera A and Schäfer H 1981 Das zustandsdiagramm Sr–Sn und die verbindung Sr_3SnO *J. Less-Common Met.* **77** 29–36

[21] Röhr C 1995 Crystal structure of calcium germanide oxide, Ca_3GeO *Z. Kristallogr.* **210** 781

[22] Huang B and Corbett J D 1998 Orthorhombic inverse perovskite Ba_3TtO ($Tt = Ge$, Si) as Zintl phases *Z. Anorg. Allg. Chem.* **624** 1787–90

[23] Velden A and Jansen M 2004 On the inverse perovskites M_3TO ($M = Ca$, Sr, Yb; $T = Si$, Ge, Sn, Pb) *Z. Anorg. Allg. Chem.* **630** 234–8

[24] Kirchner M, Schnelle W and Niewa R 2006 Inverse perovskites (Eu_3O)E with E = Sn, In—preparation, crystal structures and physical properties *Z. Anorg. Allg. Chem.* **632** 559–64

[25] Nuss J, Mühle C, Hayama K, Abdolazimi V and Takagi H 2015 Tilting structures in inverse perovskites, M_3TtO ($M = Ca$, Sr, Ba, Eu; $Tt = Si$, Ge, Sn, Pb) *Acta Cryst.* B **71** 300–12

[26] Kariyado T and Ogata M 2011 Three-dimensional Dirac electrons at the Fermi energy in cubic inverse perovskites: Ca_3PbO and its family *J. Phys. Soc. Japan* **80** 083704

[27] Kariyado T and Ogata M 2012 Low-energy effective Hamiltonian and the surface states of Ca_3PbO *J. Phys. Soc. Japan* **81** 064701

[28] Hsieh T H, Liu J and Fu L 2014 Topological crystalline insulators and Dirac octets in antiperovskites *Phys. Rev.* B **90** 081112

[29] Chiu C K, Chan Y H, Li X, Nohara Y and Schnyder A P 2017 Type-II Dirac surface states in topological crystalline insulators *Phys. Rev.* B **95** 035151

[30] Obata Y, Yukawa R, Horiba K, Kumigashira H, Toda Y, Matsuishi S and Hosono H 2017 ARPES studies of the inverse perovskite Ca$_3$PbO: experimental confirmation of a candidate 3D Dirac fermion system *Phys. Rev.* B **96** 155109

[31] Haque E and Hossain M A 2017 First-principles study of mechanical, thermodynamic, transport and superconducting properties of Sr$_3$SnO *J. Alloys Compd.* **730** 279–83

[32] Liu L G and Bassett W A 1973 Changes of the crystal structure and the lattice parameter of SrO at high pressure *J. Geophys. Res.* **78** 8470–3

[33] Samal D, Nakamura H and Takagi H 2016 Molecular beam epitaxy of three-dimensional Dirac material Sr$_3$PbO *APL Mater.* **4** 076101

[34] Chen P J and Jeng H T 2015 Phase diagram of the layered oxide SnO: GW and electron–phonon studies *Sci. Rep.* **5** 16359

[35] Haas W J, Boer S J and Berg G J 1935 The electrical resistance of cadmium, thallium and tin at low temperatures *Physica* **2** 453–9

[36] Fässler T F and Hoffmann S 2000 SrSn$_3$-a superconducting alloy with non-bonding electron pairs *Z. Anorg. Allg. Chem.* **626** 106–12

[37] Hoffmann S and Fässler T F 2003 SrSn$_4$: a superconducting stannide with localized and delocalized bond character *Inorg. Chem.* **42** 8748–54

[38] Mackenzie A P, Haselwimmer R K W, Tyler A W, Lonzarich G G, Mori Y, Nishizaki S and Maeno Y 1998 Extremely strong dependence of superconductivity on disorder in Sr$_2$RuO$_4$ *Phys. Rev. Lett.* **80** 161–4

[39] Okamoto Y, Sakamaki A and Takenaka K 2016 Thermoelectric properties of antiperovskite calcium oxides Ca$_3$PbO and Ca$_3$SnO *J. Appl. Phys.* **119** 205106